

Causes of a continuous summertime O₃ pollution event in Ji'nan, a central city in the North China Plain

Xiaopu Lyu¹, Nan Wang², Hai Guo^{1*}, Likun Xue³, Fei Jiang⁴, Yangzong Zeren¹, Hairong Cheng⁵, Zhe Cai⁴, Lihui Han⁶, Ying Zhou⁶

¹ Department of Civil and Environmental Engineering, The Hong Kong Polytechnic University, Hong Kong, China

² Division of Environmental Meteorology, Institute of Tropical and Marine Meteorology, China Meteorology Administration, Guangzhou, China

³ Environment Research Institute, Shandong University, Ji'nan, China

⁴ Jiangsu Provincial Key Laboratory of Geographic Information Science and Technology, International Institute for Earth System Science, Nanjing University, Nanjing, China

⁵ Department of Environmental Engineering, School of Resource and Environmental Sciences, Wuhan University, Wuhan, China

⁶ Department of Environmental Science, College of Environmental and Energy Engineering, Beijing University of Technology, Beijing, China

* Corresponding author: ceguohai@polyu.edu.hk

Abstract: In summer 2017, measurements of ozone (O₃) and its precursors were carried out at an urban site in Ji'nan, a central city in the North China Plain (NCP). A continuous O₃ pollution event was captured during August 4-11, with the maximum hourly O₃ reaching 154.1 ppbv. Model simulation indicated that local photochemical formation and regional transport contributed 14.0±2.3 and 18.7±4.0 ppbv/hr to O₃ increase during 09:00-15:00 local time (LT) in this event, respectively. For local O₃ formation, the calculated OH reactivity of volatile organic compounds (VOCs) and carbon monoxide (CO) was comparable between O₃ episodes and non-episodes ($p>0.05$), so was the OH reactivity of nitrogen oxides (NO_x). However, the ratio of OH reactivity of VOCs and CO to that of NO_x increased from 2.0±0.4 s⁻¹/s⁻¹ during non-episodes to 3.7±0.7 s⁻¹/s⁻¹ during O₃ episodes, which resulted in the change of O₃ formation mechanism from

the VOC-limited regime before the O₃ pollution event to the transitional regime during the event. Correspondingly, the simulated local O₃ production rate during the event (maximum: 21.3 ppbv/hr) was markedly higher than that before the event ($p < 0.05$) (maximum: 16.9 ppbv/hr). Given that gasoline and diesel exhaust made large contributions to O₃ precursors and O₃ production rate, constraint on vehicular emissions is the most effective strategy to control O₃ pollution in Ji'nan. The NCP has been confirmed as a source region of tropospheric O₃, where the widespread shift of regimes controlling O₃ formation like the case presented in this study can be expected, due to the substantial reductions of NO_x emissions in recent years.

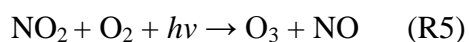
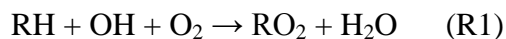
Keywords: Ozone, local formation, regional transport, volatile organic compound, North China Plain

1 Introduction

Air pollution in the North China Plain (NCP), the largest alluvial plain of China consisting of Beijing, Tianjin and many cities in Hebei, Shandong, and Henan provinces, has attracted much attention in recent years. While the annual average concentration of PM_{2.5} (particulate matters with aerodynamic diameter less than or equal to 2.5 μm) has been reduced under concerted efforts on emission restrictions (Zhang et al., 2015; Lang et al., 2017), the tropospheric ozone (O₃) pollution, which is less visible than haze but may be equivalently harmful to human health, is still severe. At a regional receptor site of the NCP in a mountainous area north of Beijing, Wang et al. (2006) reported the maximum hourly O₃ of 286 ppbv. A year-round observation of O₃ at 10 urban sites in Beijing also revealed high O₃ concentrations through May to August of 2013 (Wang et al., 2015a). Hourly O₃ mixing ratios of up to 120 ppbv were reported on Mt. Tai, the highest mountain in the NCP (1534 m a.s.l.) (Gao et al., 2005). This indicates the significant photochemical O₃ pollution over the entire NCP. Moreover, O₃ has been increasing in the NCP during the last decades (Zhang et al., 2014; Zhang et al., 2015). The increase rate of O₃ at an urban site in Beijing from 2005 to 2011 was quantified as 2.6 ppbv/year (Zhang et al., 2014), comparable to that (1.7-2.1 ppbv/year) at Mt. Tai in the summer between 2003 and 2015 (Sun et al., 2016). Overall, the NCP suffers from severe O₃ pollution, which is even aggravating.

Apart from the intrusion of stratospheric O₃ in some places with high elevations (Cooper et al., 2005; Lin et al., 2015), photochemical formation is the main source of the ground-level O₃. Volatile organic compounds (VOCs), carbon monoxide (CO) and nitrogen oxides (NO_x) are key

precursors of tropospheric O₃ (Crutzen, 1973; Chameides and Walker, 1973; Carter, 1994; Carter et al., 1995). The general chemical reactions R(1) - R(5) show the production of O₃ from the OH initiated oxidation of hydrocarbons (RH) (Jenkin et al., 1997; Atkinson, 2000; Jenkin and Clemitshaw, 2000).



The production of O₃ is generally limited by VOCs or NO_x or co-limited by both VOCs and NO_x, depending upon the chemical composition of air pollutants, particularly the relative OH reactivity of VOCs and NO_x (OH reactivity is the sum of the products of O₃ precursors concentrations and the reaction rate constants between O₃ precursors and OH). Xue et al. (2014) indicated that the summer O₃ formation was limited by NO_x in Lanzhou, consistent with Liu et al. (2010) who identified the NO_x-limited regime in most areas of northwest China. In the southwest, O₃ formation was diagnosed as VOC-limited in Chengdu, but NO_x-limited in Pengzhou due to the large quantities of emissions from petrochemical industry (Tan et al., 2018a). Lyu et al. (2016) reported the VOC-limited regime in Wuhan, central China. The VOC-limited regime has also been repeatedly confirmed for O₃ formation in Shanghai (Xue et al., 2014; Xing et al., 2017) and Nanjing (Ding et al., 2013), eastern China. In the Pearl River Delta of southern China, it was found that O₃ formation was generally limited by VOCs in the southwest, while limited by NO_x in the northeast (Ye et al., 2016). In the NCP, both Han et al. (2018) and Xing et al. (2018) summarized that VOCs limited O₃ formation in most urban areas. However, in the suburban and rural areas, O₃ formation was generally in the transitional regime, *e.g.* Yucheng (Zong et al., 2018), or limited by NO_x, *e.g.* Wangdu (Tan et al., 2018b). From a historical perspective, Jin et al. (2017) pointed out that the sensitivity of O₃ formation to VOCs increased in most Chinese cities, however decreased in some megacities (such as Beijing and Shanghai) due to the stringent control of NO_x emissions in recent years. Different VOCs play non-equivalent roles in O₃ formation. Alkenes, aromatics and carbonyls can be readily oxidized by oxidative radicals (*e.g.* OH) or photolyzed (applicable for carbonyls), leading to O₃ formation (Cheng et al., 2010; Guo

et al., 2013). Therefore, the sources with a bulk emission of these VOCs generally make considerable contributions to the photochemical production of ground-level O₃. For example, Cheng et al. (2010) pointed out that carbonyls increased the peak O₃ production rates at a rural site and a suburban site in South China by 64% and 47%, respectively. Solvent based industry and paint solvent usage with high emissions of aromatics were responsible for more than half of O₃ formation potential in Shanghai (Cai et al., 2010). Carbonyls and alkenes accounted for 71-85% of the total OH reactivity of VOCs in Beijing (Shao et al., 2009).

In addition to the chemical processes, O₃ pollution is also closely associated with meteorological conditions, which influence the formation, transport and accumulation of O₃. Studies (Chan and Chan, 2000; Huang et al., 2005) indicated that tropical cyclone (typhoon) and continental anticyclone are the most common synoptic systems conducive of O₃ pollution in coastal cities of southern China. Many O₃ episodes in eastern China occurred under the control of the west Pacific subtropical high pressure (He et al., 2012; Shu et al., 2016). In the NCP, the summertime O₃ pollution is generally accompanied with a weak high pressure system (Wang et al., 2010). Furthermore, the terrain also plays a role in O₃ pollution. For example, the mountains in north and west of Beijing lead to upslope winds (valley breeze) in daytime, transporting polluted air masses laden with O₃ from the NCP to Beijing (Lin et al., 2008). Overall, the causes of O₃ pollution are generally complicated and need to be analyzed case by case.

The NCP is the region with the largest emission amount of air pollutants in China (Gu et al., 2014; Li et al., 2017), partially accounting for the severe O₃ pollution there. In addition, O₃ pollution in the NCP is closely related to the synoptic systems and topographic features (Chen et al., 2009; Zhang et al., 2016). For example, the strong photochemical production of O₃ in urban plumes of Beijing was found by Wang et al. (2006), while the contribution of regional transport was revealed by the enhanced O₃ production at a rural site in the NCP under southerly winds (Lin et al., 2008). Through the review of synoptic systems in the NCP from 1980 to 2013, Zhang et al. (2016) concluded that the air quality was generally unhealthy under weak East Asian Monsoons. Moreover, a decadal statistical analysis indicated that meteorological factors explained ~50% of the O₃ variations in Beijing (Zhang et al., 2015). Despite many previous studies, the evolutions of the synoptic and photochemical processes in O₃ pollution events, and their contributions to the non-attainment of O₃ have been seldom looked into in the NCP.

Besides, the local and regional contributions to the elevated O_3 in the NCP are not unambiguously quantified, limited by the deficiencies in model representation of either physical or local chemical processes. The situation was even much worse for Ji'nan, the capital of Shandong province. As early as 2000s, studies (Shan et al., 2008; Yin et al., 2009) reported the maximum hourly O_3 of 143.8 ppbv and 147.8 ppbv in June 2004 and 2005, respectively. Even higher O_3 (198 ppbv) was observed at a rural site downwind of Ji'nan in June 2013 (Zong et al., 2018). However, almost no study was carried out to explore the mechanisms responsible for high O_3 there, though it has been confirmed that air pollution in the NCP cities like Ji'nan influenced air quality in Beijing (Lin et al., 2008; Wang et al., 2010). To better understand O_3 pollution in the NCP, this study investigated the causes of an O_3 episode lasting for eight days in Ji'nan in the summer of 2017. The analyses presented here focus on the synoptic systems dominating Shandong Peninsula during this event; the chemical profiles of O_3 and O_3 precursors; and the simulation of factors contributing to O_3 in Ji'nan with the aid of a chemical transport model and a photochemical box model. In addition, we propose feasible O_3 control measures based on the source-resolved OH reactivity of VOCs and NO_x .

2 Methodology

2.1 Site description

The air quality monitoring and sample collection were carried out on the rooftop of a 7-story building on the campus of Shandong University from July 15 to August 14, 2017. The campus is located in the urban area of Ji'nan, and the site is about 50 m from a main road (Shanda South Road) outside the campus. Figure 1 shows the locations of the sampling site (36.68°N, 117.07°E, 22 m a.g.l.) and some surrounding urban air quality monitoring stations (AQMSs) set up by China National Environmental Monitoring Center (CNEMC). Also shown are the observed O_3 and monitored rainfall averaged over August 4-11, 2017 when O_3 episodes occurred in Ji'nan. It is noteworthy that the days with maximum hourly O_3 exceeding 100 ppbv (Grade II of National Ambient Air Quality Standard) were defined as O_3 episode days. O_3 data in hourly resolution at the AQMSs were obtained from the website of CNEMC (<http://www.cnemc.cn/>). The high O_3 at almost all the AQMSs in the NCP (Figure 1 (a)) indicated a regional O_3 pollution event in this period. The regional-wide homogeneity was to some extent represented by the observations at

the sampling site, in view of the comparable O_3 levels. This was confirmed by the strong influences of regional transport on O_3 variations at the site, as discussed in section 3.3.

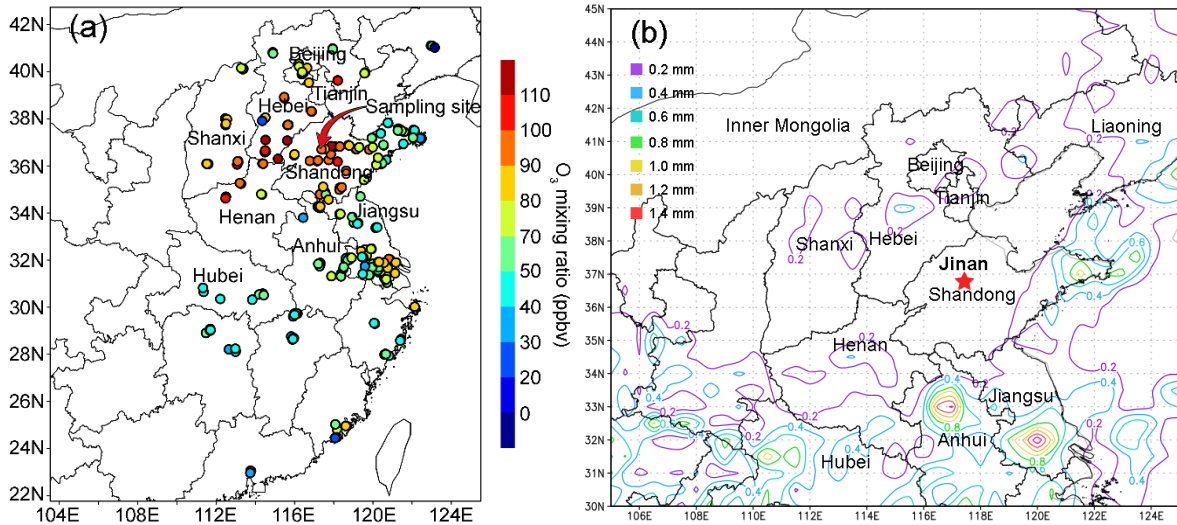


Figure 1 (a) Locations of the sampling site and the CNEMC AQMSs, and the average observed O_3 at 14:00 LT on August 4-11, 2017 (colored circles). The sampling site is overlapped with the nearest AQMS in Ji'nan. (b) Rainfall distribution, in millimeters (mm), averaged over August 4-11, 2017.

2.2 Air quality monitoring and sample collection

2.2.1 Continuous monitoring of air pollutants and meteorological parameters

O_3 , NO and NO_2 were continuously monitored at the sampling site between July 15 and August 14, 2017. The air was drawn through a 4 m Teflon tube by the pumps in the trace gas analyzers with the total flow rate of 2 L/min (1.4 L/min for O_3 analyzer and 0.6 L/min for NO_x analyzer). The inlet was located ~1 m above the rooftop of the 7-story building (~22 m a.g.l.). O_3 and NO/ NO_x were detected with a UV photometric based analyzer and a chemiluminescence NO- NO_2 - NO_x analyzer, respectively (see Table S1 for the specifications). The lowest NO observed during the sampling period was 2.4 ppbv, 6 times (600% of) the lower detection of the NO_x analyzer (0.4 ppbv). Taking the measurement accuracy of <15% into consideration, we believe that the NO measurements were basically reliable. NO_2 was calculated from the difference between NO and NO_x . Studies indicated that NO_2 monitored with chemiluminescence was generally overestimated due to the conversion of the total odd nitrogen (NO_y) to NO by

molybdenum oxide catalysts (McClenny et al., 2002; Dunlea et al., 2007; Xu et al., 2013). The positive bias was more significant in more aged air masses, resulting from higher levels of NO_z ($\text{NO}_z = \text{NO}_y - \text{NO}_x$) (Dunlea et al., 2007). The average overestimation of NO_2 was 22% in Mexico City, which even increased to 50% in the afternoon (Dunlea et al., 2007). Xu et al. (2013) suggested that the chemiluminescence monitors overestimated NO_2 by less than 10% in urban areas with fresh emission of NO_x , but the positive bias went up to 30-50% at the suburban sites. As described in section 2.1, our sampling site was located in the urban area of Ji'nan and was only ~50 m to a main road. Therefore, we infer that NO_2 might not be significantly overestimated in this study. However, the larger overestimations could be expected during O_3 episodes, because the stronger photochemical reactions enhanced the productions of many NO_z species. We adopted 30% (minimum bias in suburban area) and 10% (maximum bias in urban area) as the maximum fraction of NO_2 overestimation during episodes and non-episodes at this urban site, respectively. The influences of the NO_2 measurement interferences on the results were discussed where necessary.

The hourly concentrations of sulfur dioxide (SO_2) and CO were acquired from a nearest AQMS of CNEMC which is ~1 km from our sampling site. Year-round monitoring of inorganic trace gases was conducted at this AQMS, where the air was drawn into the analytical instruments at a flow rate of 3 L/min through an inlet, ~1 m above the rooftop of a 5-story building (~ 16 m a.g.l.). The specifications of the instruments deployed at the AQMS are also provided in Table S1. The hourly concentrations of O_3 and NO_2 measured at our sampling site agreed well with those reported at the AQMS (NO data was not available on CNEMC website), with the slope of 1.04 ($R^2 = 0.82$) and 1.13 ($R^2 = 0.71$) for O_3 and NO_2 in the linear least square regressions, respectively (Figure S1). Due to the instrumental differences and/or differences in sources and sinks of air pollutants at the two sites, the agreements were worse at low mixing ratios for both O_3 and NO_2 . Therefore, we only used SO_2 and CO monitored at the nearest AQMS in this study, which had lower photochemical reactivity than O_3 and NO_2 , and were more homogeneous at a larger scale.

In addition, the meteorological parameters, including wind speed, wind direction, pressure, temperature and relative humidity, were monitored at the sampling site by a widely used weather station (China Huayun group, Model CAWS600-B). The daily total solar radiation was obtained

from the observations at a meteorological station in Ji'nan (36.6 °N, 117.05 °E, 170.3 m a.s.l), 9 km to our sampling site.

2.2.2 Sample collection and chemical analysis

The VOC and oxygenated VOC (OVOC) samples were collected on 9 selective days (*i.e.*, July 20 and 30, August 1, 4-7 and 10-11), referred to as VOC sampling days hereafter. The days were selected to cover the periods with relatively high and low levels of O₃. The high O₃ days were forecasted prior to sampling based on the numerical simulations of meteorological conditions and air quality. In total, 6 out of 9 VOC sampling days were O₃ episode days with the maximum hourly O₃ ranging from 100.4 to 154.1 ppbv. On each day (regardless of episode or non-episode), 6 VOC/OVOC samples were collected between 08:00 and 18:00 LT every 2 hours with the duration of 1 hour for VOC and 2 hours for OVOC samples. VOC samples were collected with 2 L stainless steel canisters which were cleaned and evacuated before sampling. A flow restrictor was connected to the inlet of the canister to guarantee 1 hour sampling. OVOC were sampled with the 2,4-dinitrophenylhydrazine (DNPH) cartridge, in front of which an O₃ scrubber was interfaced to remove O₃ in the air. A pump behind the DNPH cartridge drew the air at a flow of 500 L/min. After sampling, all the DNPH cartridges were stored in a refrigerator at 4 °C until chemical analysis.

VOC samples were analyzed with a gas chromatograph-mass selective detector/flame ion detector/electron capture detector system (Colman et al., 2001). In total, 85 VOCs, including 59 hydrocarbons, 19 halocarbons and 7 alkyl nitrates, were quantified. The overall ranges of the detection limit (DL), accuracy and precision for VOCs analysis were 1-154 pptv, 1.2-19.8% and 0.1-17.9%, respectively. The analysis results given by this system have been compared with those analyzed by UCI and good agreements were achieved (Figure S2). OVOC samples were eluted with 5 mL acetonitrile, followed by analysis with the high performance liquid chromatography. The DL, accuracy and precision for all OVOCs analysis were within the range of 3-11 pptv, 0.32-0.98% and 0.01-1.03%, respectively.

2.3 Model configuration

2.3.1 Chemical transport model

To analyze the processes contributing to high O₃ in Ji'nan, a chemical transport model, the Weather Research Forecast-Community Multi-scale Air Quality (WRF-CMAQ), was utilized to simulate O₃ in this study. WRF v3.6.1 was run to provide the offline meteorological field for CMAQ v5.0.2. A two-nested domain was adopted with the resolution of 36 km (outer domain) and 12 km (inner domain), respectively. As shown in Figure S3, the outer domain covered the entire continental area of China aiming to provide sufficient boundary conditions for the inner domain, which specifically focused on eastern China.

We used the 2012-based Multi-resolution Emission Inventory for China (MEIC) to provide anthropogenic emissions of air pollutants, which was developed by Tsinghua University specific for China, with the grid resolution of 0.25 °×0.25 ° (Zhang et al., 2007; He, 2012). Five emission sectors, namely transportation, agriculture, power plant, industry and residence were included in MEIC. The emission inventory was linearly interpolated to the domains with consideration of the earth curvature effect. For grids outside China, the air pollutant emissions were derived from INTEX-B (Intercontinental Chemical Transport Experiment-Phase B) Asian emission inventory (Zhang et al., 2009). Consistent with many previous studies (Jiang et al., 2010; Wang et al., 2015b), the Model of Emissions of Gases and Aerosols from Nature (MEGAN) was used to calculate the biogenic emissions. The physical and chemical parameterizations for WRF-CMAQ were generally identical to those described in Wang et al. (2015b), with some improvements. Firstly, the carbon bond v5 with updated toluene chemistry (CB05-TU) was chosen as the gas phase chemical mechanism (Whitten et al., 2010). Secondly, a single-layer urban canopy model (Kusaka and Kimura, 2004) was used to model the urban surface-atmosphere interactions. Thirdly, the default 1990s U.S. Geological Survey data in WRF was replaced by adopting the 2012-based moderate resolution imaging spectroradiometer (MODIS) land cover data for eastern China. The substitution was performed to update the simulation of boundary meteorological conditions (Wang et al., 2007).

An integrated process rate (IPR) module incorporated in CMAQ was used to analyze the processes influencing O₃ concentration. Through solving the mass continuity equation established between the overall change of O₃ concentration with time and the change of O₃ concentration caused by individual processes, including horizontal diffusion (HDIF), horizontal advection (HADV), vertical diffusion (VDIF), vertical advection (VADV), dry deposition

(DDEP), net effect of chemistry (CHEM) and cloud processes (CLD), the contributions of the processes to O_3 variation rate were determined. Note that the estimate of CHEM is influenced by the estimate of O_3 precursor emissions, the simulation of meteorological conditions and the chemical mechanism, all the three aspects should be taken into account wherever CHEM is discussed. The IPR analysis has been widely applied in process diagnosis of O_3 pollution (Huang et al., 2005; Wang et al., 2015b). Since the field observations were conducted near the surface (~22 m a.g.l.), and the box model introduced below was constrained by the observations, the modeling results on the ground-level layer were extracted from WRF-CMAQ for analyses in this study.

2.3.2 Photochemical box model

A Photochemical Box Model incorporating the Master Chemical Mechanism (PBM-MCM) was used to study the in situ O_3 chemistry, in view of the detailed (species-based) descriptions of VOC degradations in the MCM (Saunders et al., 2003; Lam et al., 2013). The PBM model was localized to be applicable in Ji'nan, with the settings of geographic coordinates, sunlight duration and photolysis rates. The photolysis rates were calculated by the TUV model (Madronich and Floke, 1997). Specifically, the geographical coordinates, date and time were input into the TUV model, initializing the calculation of solar radiation with the default aerosol optical depth (AOD), cloud optical depth (COD), surface albedo and other parameters. Then, COD was adjusted to make the calculated daily total solar radiation progressively closer to the observed value. When the difference between the calculated and observed solar radiation were less than 1%, the input parameters with the adjusted COD were accepted. Based on the settings, the hourly solar radiations and the photolysis rates of O_3 ($J(O^1D)$) and NO_2 (JNO_2) were calculated by the TUV model, and applied to PBM-MCM for O_3 chemistry modelling. Table S2 shows the daily maximum $J(O^1D)$ and JNO_2 on the VOC sampling days. The MCM v3.2 (<http://mcm.leeds.ac.uk/MCM/>) used in the present model consists of 17,242 reactions among 5,836 species. The measurements of O_3 and its precursors at 00:00 on each day were used as the initial conditions for each day's modelling. The initial O_3 , as the O_3 left over from the days before the modelling day, accounted for a part of the primary OH production. Hourly concentrations of 46 VOCs, 4 OVOCs and 4 trace gases (SO_2 , CO, NO and NO_2), as well as hourly meteorological parameters (temperature and relative humidity) were input into the model,

so that the model was constrained to observations. The hourly observed O₃ were not input, as it was the species to be modeled. The Freon, cycloalkanes and methyl cycloalkanes with low O₃ formation potentials were not included in model input. Also omitted were the species whose concentrations were lower than the detection limits in more than 20% of the samples, such as the methyl hexane and methyl heptane isomers. For the hours when measurement data were not available, the concentrations were obtained with linear interpolation. Some secondary species, such as formaldehyde (HCHO), acetaldehyde and acetone, were input into the model to constrain the simulation. Since other secondary species, *e.g.*, PAN and HNO₃ were not observed in this study, their concentrations were calculated by the model. Dry deposition was considered for all the chemicals by setting the deposition velocities identical to those in Lam et al. (2013). Since NO and NO₂ were separately measured and input into the model, they experienced different reactions as described by the species-based chemical mechanisms.

The simulations were separately carried out on all the VOC sampling days. To spin-up the model, the concentrations of air pollutants and meteorological conditions which were the same as those on the day of interest were input into the model for 72-h simulation before the modelling on that day. The model treated the air pollutants to be well-mixed in the boundary layer, without consideration of dilution and transport. O₃ in the free troposphere was not considered either, due to the lack of O₃ observations above the boundary layer over Ji'nan. This might hinder the accurate reproduction of the observed O₃, particularly on the days when advection and diffusion were strong. Since the model mainly described the in situ photochemistry, it was validated through comparison with the CHEM process simulated by WRF-CMAQ. The simulated O₃ production rates were output every hour, which were integrated values over every 3600 s (model resolution: 1 s). More details about the model configuration can be found in Lam et al. (2003) and Lyu et al. (2017).

3. Results and discussion

3.1 Overall characteristics of O₃ pollution in Ji'nan

Figure 2 shows the time series of trace gases, the OH reactivity of VOCs, CO and NO_x, and meteorological conditions on the VOC sampling days in Ji'nan (Trace gases in the whole sampling period are shown in Figure S4). All the OH reactivity values discussed in this study were calculated rather than observed. The OH reactivity values of VOCs are grouped into those

of carbonyls, biogenic VOCs (BVOCs), aromatics, alkenes and alkanes (Table S3 lists the VOCs included in each group). The reaction rate constants between O_3 precursors and OH in calculation of OH reactivity were adopted from the MCM v3.2 (<http://mcm.leeds.ac.uk/MCM/>). The average total OH reactivity on all the VOC sampling days ($19.4 \pm 2.1 \text{ s}^{-1}$) was comparable to that reported in New York ($19 \pm 3 \text{ s}^{-1}$, Ren et al., 2003), Houston ($9\text{--}22 \text{ s}^{-1}$, Mao et al., 2010) and Beijing ($15\text{--}27 \text{ s}^{-1}$, Williams et al., 2016). Consistent with the previous studies in urban areas (Ren et al., 2003; Yang et al., 2016 and references therein), NO_x was the largest contributor ($28.9 \pm 1.9\%$) to the total OH reactivity. Noticeably, $20.5 \pm 4.1\%$ of the total OH reactivity was attributable to BVOCs, which was much higher than the contributions in urban areas ($<10\%$) reviewed by Yang et al. (2016). The elevated isoprene levels (2.2 ± 0.6 ppbv during episodes and 0.9 ± 0.3 ppbv during non-episodes) under high temperature (mean: 31°C) explained the considerable contribution of BVOCs to the total OH reactivity in this study.

O_3 episodes were captured on 6 out of the 9 VOC sampling days, with the highest O_3 of 154.1 ppbv at 13:00 LT on August 10. It was found that the total OH reactivity of VOCs and CO ($OH \text{ reactivity}_{VOCs+CO}$) was comparable between O_3 episodes ($14.8 \pm 2.0 \text{ s}^{-1}$) and non-episodes ($12.2 \pm 3.0 \text{ s}^{-1}$), so was the OH reactivity of NO_x ($4.7 \pm 0.8 \text{ s}^{-1}$ and $6.9 \pm 1.9 \text{ s}^{-1}$ during episodes and non-episodes, respectively). Taking the positive biases of NO_2 measurement into account (section 2.2.1), we found that the OH reactivity of NO_x was overestimated by the maximum of $17.5 \pm 1.1\%$ and $5.4 \pm 0.7\%$ during O_3 episodes and non-episodes, respectively. In the case of maximum overestimations, the actual OH reactivity of NO_x during episodes ($4.0 \pm 0.7 \text{ s}^{-1}$) might be lower ($p < 0.05$) than that during non-episodes ($6.6 \pm 1.9 \text{ s}^{-1}$). The high OH reactivity during non-episodes mainly occurred on July 30 and August 1, due to the high pressure, weak solar radiation and low temperature. Despite the comparable OH reactivity, we found that the ratio of $\frac{OH \text{ reactivity}_{VOCs+CO}}{OH \text{ reactivity}_{NOx}}$ during O_3 episodes ($3.7 \pm 0.7 \text{ s}^{-1}/\text{s}^{-1}$) was higher ($p < 0.05$) than during non-episodes ($2.0 \pm 0.4 \text{ s}^{-1}/\text{s}^{-1}$). It was likely that the difference was even larger, due to the more significant overestimation of NO_2 during episodes. This indicated that O_3 formation was more limited by VOCs during non-episodes than during episodes. In fact, O_3 formation in Ji'nan switched to the transitional regime during episodes from the VOC-limited regime during non-episodes (see section 3.4.2). This partially explained the building-up of O_3 on episode days, as O_3 productions were generally the highest in the transitional regime.

From the perspective of meteorological conditions, O₃ episodes had relatively stronger solar radiation, higher temperature, lower relative humidity and weaker winds ($p<0.05$). This is reasonable as O₃ formation and accumulation are generally enhanced under these weather conditions. As aforementioned, the solar radiation on July 30 was much weaker than those during O₃ episodes, which was probably the most critical factor leading to low O₃ on this day. Figure S5 shows the COD retrieved from the terra/MODIS (https://ladsweb.modaps.eosdis.nasa.gov/search/imageViewer/1/MOD06_L2--61/2017-08-06/DB/Site:142/2873994172--3) at 10:00 – 12:00 LT of the VOC sampling days. The terra/MODIS image revealed thick cloud cover with high COD over Ji'nan on July 30, explaining the weak solar radiation. In fact, obvious anti-correlation existed between solar radiation and the COD. The influences of cloud cover/ COD and solar radiation on O₃ pollution during the study period in Ji'nan are discussed in section 3.2. Unlike many previous findings that O₃ pollution was aggravated by high pressure (Chan and Chan, 2000; Zhao et al., 2009), the sea-level pressure during O₃ episodes (993.4 ± 0.2 hPa) was significantly lower than during non-episodes (996.1 ± 0.4 hPa) in this study ($p<0.05$). When O₃ reached its hourly maximum on August 10 (154.1 ppbv), the pressure was at its lowest value (990.2 hPa). The continuously severe O₃ pollution event under low pressure is further investigated below.

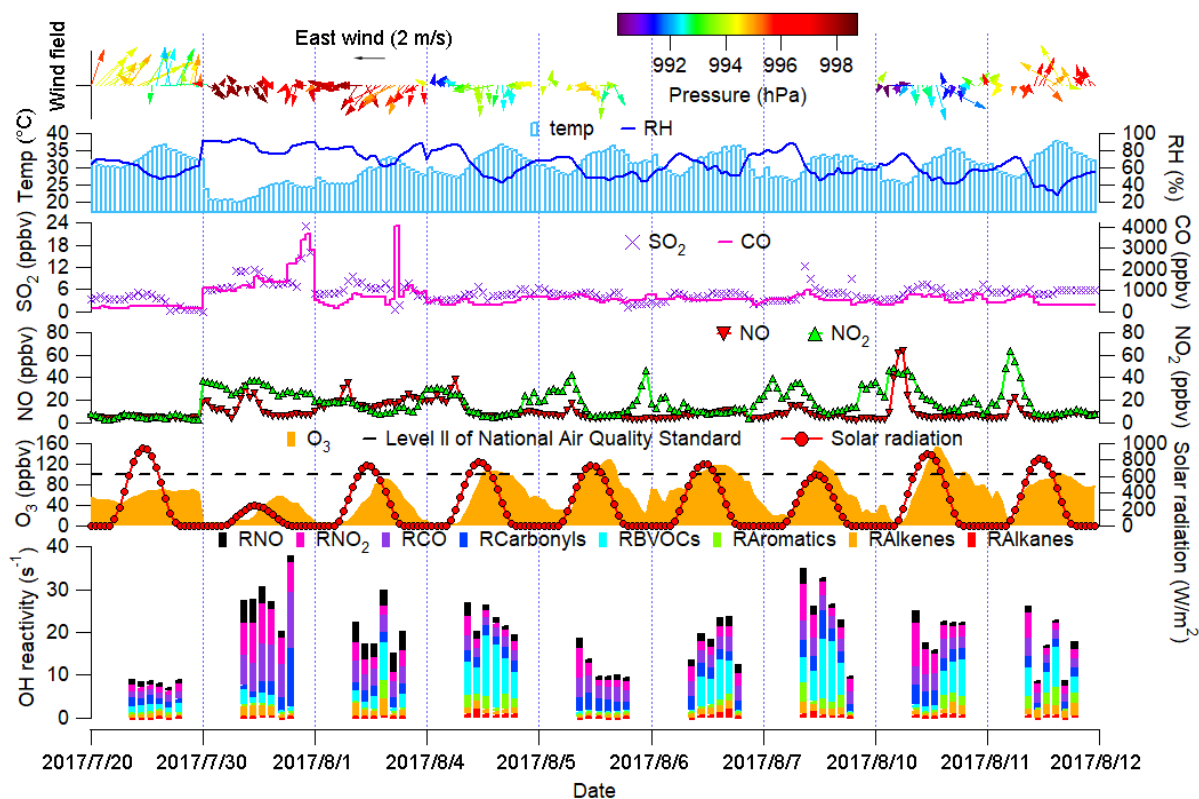


Figure 2 Time series of trace gases, OH reactivity of O₃ precursors and meteorological parameters. Wind speed and wind direction were not monitored from 17:00 LT on August 5 to 23:00 LT on August 7 due to malfunction of the weather station. RX in the bottom panel is the OH reactivity of species/group X.

3.2 Synoptic processes and relationship with O₃ pollution

Obviously, this O₃ pollution event was accompanied by unique weather conditions (*e.g.* low pressure on high O₃ days), which needed to be further studied. Figure 3 displays the average weather charts at 14:00 LT during O₃ episodes and non-episodes (weather charts on individual VOC sampling days are shown in Figure S6). Clearly, the temperature over Shandong Peninsula was much higher during O₃ episodes than non-episodes, which favored O₃ formation on episode days. Additionally, southerly and southwesterly winds originating from the inland areas (Hubei, Henan, and Anhui provinces) prevailed in central and western Shandong province during O₃ episodes. In contrast, the winds were generally from the sea or coastal region in Jiangsu province during non-episodes. O₃ and O₃ precursors might be transported to Ji'nan in the former cases. Though the winds were from the relatively clean sea and coastal regions during non-episodes,

the concentrations of O₃ precursors on July 30 and August 1 were still high, which were mainly caused by weather conditions (high pressure, low temperature and low solar radiation), as discussed in section 3.1. Further, we also noted that the winds changed direction from southwest to northwest around Ji'nan during O₃ episodes. This meant that there might be a local circulation hampering the dispersion of air pollutants during episodes. It seems that the turning-round of the winds around Ji'nan was associated with the sea breeze from Bohai Bay. This was very similar to the convergence of continental air and sea breeze (from South China Sea) in Pearl River Delta (Fung et al., 2005; Lo et al., 2006). Overall, the wind fields were more favorable for regional transport and accumulation of air pollutants in Ji'nan during O₃ episodes. In addition, Shandong Peninsula was under a uniform pressure field with the sea-level pressure of 1000-1001 hPa during O₃ episodes, implying the relatively stagnant weather conditions unfavorable for the dispersion of air pollutants.

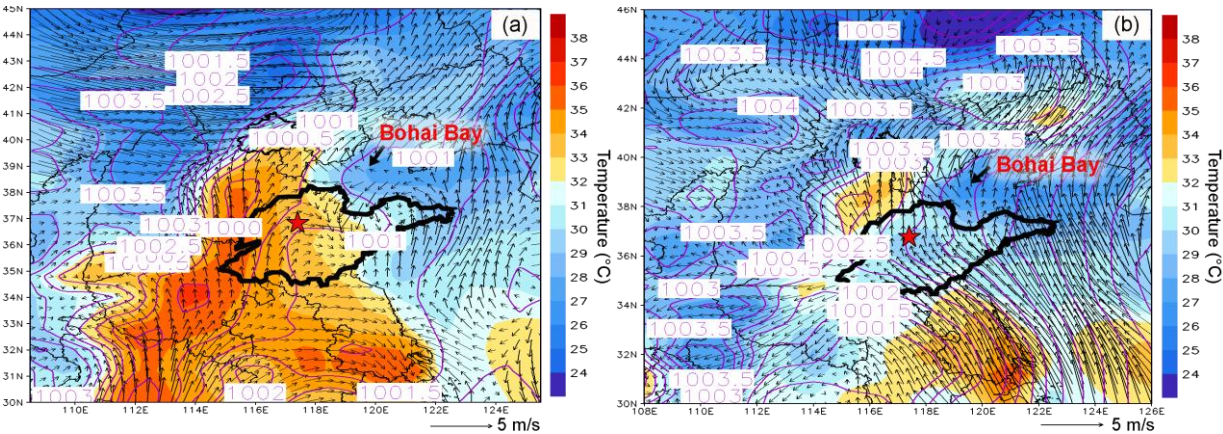


Figure 3 Weather chart at 14:00 LT averaged over (a) O₃ episodes and (b) non-episodes. The red star represents Ji'nan. The dark black line is the boundary of Shandong province. Bohai Bay is located to the northeast of Shandong province. Numbers in the figure are sea-level pressures in unit of hPa.

To better understand the relationship between O₃ pollution and the synoptic systems, Table 1 summarizes the synoptic systems, weather conditions and air mass origins on all the VOC sampling days. The weather charts at surface level and 500 hPa on August 1, 4, 7, 10 and 13 are presented in Figures S7-S8, showing the evolution of the synoptic systems. To identify the origins of air masses, the 48 hour backward trajectories of air masses are shown in Figure 4. The trajectories were computed using the Hybrid Single Particle Lagrangian Integrated Trajectory

(HYSPLIT) Model v 4.9. Each trajectory was calculated for 48 hours and the calculation was done every 6 hours (4 trajectories each day). Our sampling site (36.68 N, 117.07 E) was set as the starting point of the backward trajectories with the height of 500 m a.s.l. The discrepancy between the wind direction and origin of air masses, *e.g.* on August 1 and 11, was likely due to the air recirculation at the ground level.

It was found that Ji'nan was under the control of the Western Pacific Subtropical High (WPSH) on July 20 (weather chart on 500 hPa is not shown here), and the air masses arriving in Ji'nan originated from South China 48 hours prior (Figure 4). As anticipated, the WPSH caused high temperatures and the intensive solar radiation during the study period (maximum: 943 W/m²) in Ji'nan (Figure 2), which was conducive to O₃ formation. However, the winds on July 20 were the strongest in the entire VOC sampling period, with the highest hourly wind speed of 3.9 m/s. The strong winds facilitated the transport and dispersion of O₃ precursors and locally formed O₃ on July 20 (refer to the low levels of O₃, O₃ precursors and OH reactivity in Figure 2). The WPSH moved southward on the following days and Ji'nan was under a uniform pressure field, which was formed in the peripheries of two low pressure systems (two rain belts as shown in Figure 1), *i.e.* one over Central China and another over North China (Figure S7). Thus, the pressure in Ji'nan was relatively high (997.1±0.3 hPa), compared to the south and north regions. This synoptic system lasted for several days until August 7, covering 2 non-episode days and 4 O₃ episode days. The low O₃ values on July 30 and August 1 were mainly attributable to the weak solar radiation and low temperature as discussed above.

In contrast, continuously strong solar radiation with low COD (Figure 2 and Figure S5), high temperature and continental air masses (Figure 4) were observed on August 4-7. This, in addition to the shift of O₃ formation mechanism (see sections 3.1 and 3.4.2), explained the prolonged O₃ pollution event. On August 10, the rain belt over North China moved southward, forming a deep low pressure trough over the NCP and Ji'nan was behind the trough (Figure S8 (d)). The low pressure trough is a typical synoptic system conducive of O₃ pollution, resulting from the intrusion of O₃ in the stratosphere and/or the upper troposphere (Chan and Chan, 2000). Moreover, there was nearly no cloud cover over the entire NCP on August 10 (Figure S5). Consequently, the highest O₃ (154.1 ppbv) in this sampling campaign was observed on August 10. On August 11, the low pressure system continued to extend to the Yellow Sea. O₃ decreased

substantially on this day with the disappearance of the low pressure trough and the weakening of solar radiation, though the hourly maximum O₃ still reached 100.4 ppbv. On the following days, the precipitations relieved the O₃ pollution in Ji'nan.

Table 1 Summary of the synoptic systems, weather conditions and air mass origins on VOC sampling days.

Date	O ₃ maximum (ppbv)	Episode/non-episode	Synoptic system Weather condition	Air mass origin
July 20	71.0	Non-episode	WPSH, strong southwesterly winds	Continental air masses from South China
July 30	57.6		Uniform pressure field (weak high pressure), rain, fog, calm winds	Marine air masses
August 1	90.6		Uniform pressure field (weak high pressure), northeasterly winds	
August 4	107.5	Episode	Uniform pressure field (weak high pressure), northeasterly winds	Continental air masses from Shandong province
August 5	128.2		Uniform pressure field (weak high pressure), calm winds	
August 6	116.9		Uniform pressure field (weak high pressure), southwesterly winds	
August 7	126.9		Uniform pressure field (weak high pressure), calm winds	Continental air masses from the north
August 10	154.1		Low-pressure trough, calm winds	Continental air masses from the west
August 11	100.4		Subtropical high, southeasterly winds	Continental air masses from the southwest

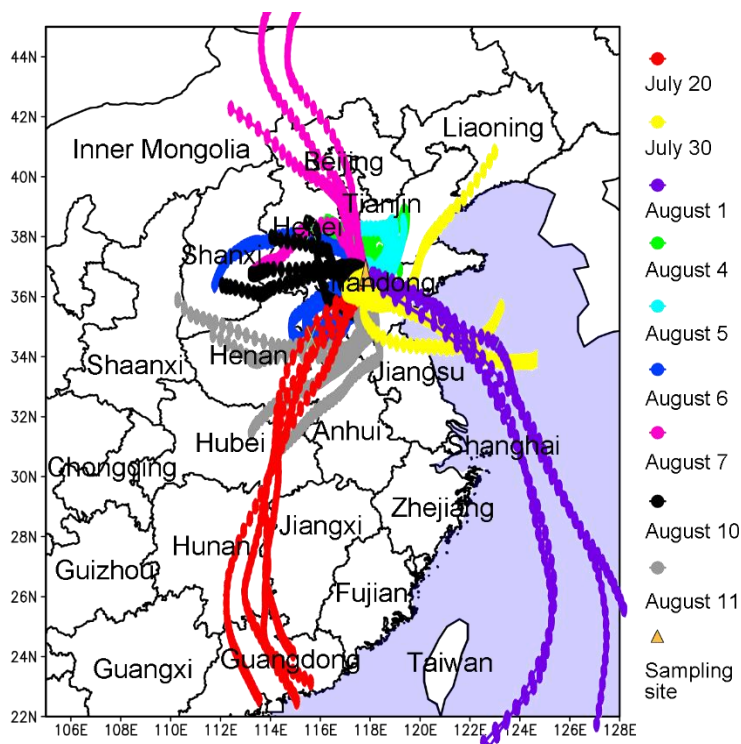


Figure 4 Forty eight hour backward trajectories calculated every 6 hours, with Ji'nan (36.68 N, 117.07 E, 500 m a.g.l.) as the starting point. The trajectories are simulated by HYSPLIT v4.9. The water areas are highlighted in blue.

3.3 O₃ simulation and process analysis

The observations indicated the likely different regimes controlling local O₃ formation and the potential impacts of regional transport. To understand the atmospheric chemistry and dynamics, as well as their roles in this O₃ pollution event, the WRF-CMAQ was applied. Figure 5 shows the hourly average simulated and observed O₃ on the VOC sampling days in Ji'nan. Overall, the model well reproduced the magnitudes and diurnal patterns of the observed O₃, except for the higher simulated O₃ on July 20 and the under-prediction of O₃ on August 1, 7 and 10. Discussions on the discrepancies and the detailed model validation are provided in Text S1, Figures S9-S11 and Table S4.

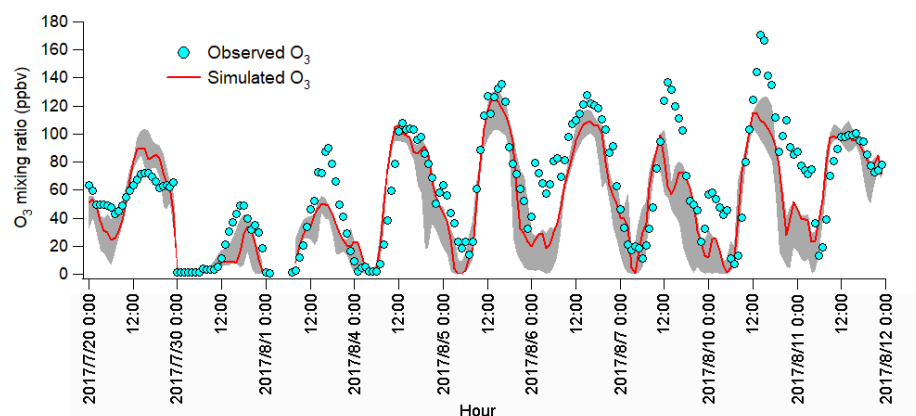


Figure 5 Hourly average mixing ratios of the WRF-CMAQ simulated and observed O₃ in Ji'nan. The grey area shows the minimum and maximum simulated O₃ at the sampling site and 8 adjoining grids (12×12 km² for each grid).

The IPR analysis quantifies the contributions of different processes to the O₃ production rate, as shown in Figure 6. HDIF and HADV were summed as horizontal transport (HTRA), and the vertical transport (VTRA) was a total representative of VDIF and VADV. It was found that chemical reactions generally led to O₃ decrease during non-episodes. The negative contributions of chemical reactions on July 20 coincided with the very low concentrations of O₃ precursors and the flat diurnal cycle of O₃ (Figure 2). The chemical destruction of O₃ on July 30 and August 1 was most likely related to the relatively weak solar radiation and low temperature, which inhibited the in situ photochemical reactions. In fact, the negative chemical effect should be considered as the titration of NO to regionally-transported and/or background O₃ and the depletion of O₃ by the freshly emitted NO near the sources (Beck and Grennfelt, 1994; Sillman, 1999). Conversely, the combined effect of horizontal and vertical transport was to increase O₃.

During O₃ episodes, chemical reactions made positive contributions to O₃ production between 09:00 LT and 15:00 LT, with the average hourly O₃ production rate of 14.0 ± 2.3 ppbv/hr. At the same time, O₃ was also elevated by transport at an average rate of 18.7 ± 4.0 ppbv/hr, as a combined effect of vertical transport (-40.8 ± 20.2 ppbv/hr) and horizontal transport (59.5 ± 19.8 ppbv/hr). The negative contribution of vertical transport to O₃ in these hours might be caused by the updraft with the increase of temperature in the city. The O₃ enhancement by horizontal transport could be explained by the westerly to northerly airflows and the high O₃ in the NCP where the airflows originated or passed (Figure 4 and Figure S10). The much higher O₃ over the

NCP than in the surrounding regions indicated that the NCP was an O₃ source in this case. In fact, the transport of O₃ from the lower troposphere over the NCP to the free troposphere and further to northeast China was also presented by Ding et al. (2009).

During 16:00-08:00 LT on O₃ episode days, O₃ was titrated and chemically consumed at the rate of 49.4 ± 6.3 ppbv/hr. This was reasonable in view of the fresh vehicular emissions (particularly NO_x) in the morning and evening rush hours, when the titration of O₃ by NO produced NO₂. The NO₂ was carried over to the other places by air circulation, and/or oxidized to NO₃ and N₂O₅, which could further react with aerosol to form HNO₃ and ClNO₂ in the evening. Horizontal and vertical transport dominated O₃ sources, with the average positive contribution of 5.7 ± 7.0 and 54.5 ± 9.6 ppbv/hr during 16:00-08:00 LT on August 4-11, respectively. The strong vertical transport coincided with the downward winds in the evening, which brought the high-altitude O₃ to the ground, as indicated in Figure S9. However, the sources of O₃ in the upper atmosphere were beyond the scope of this study.

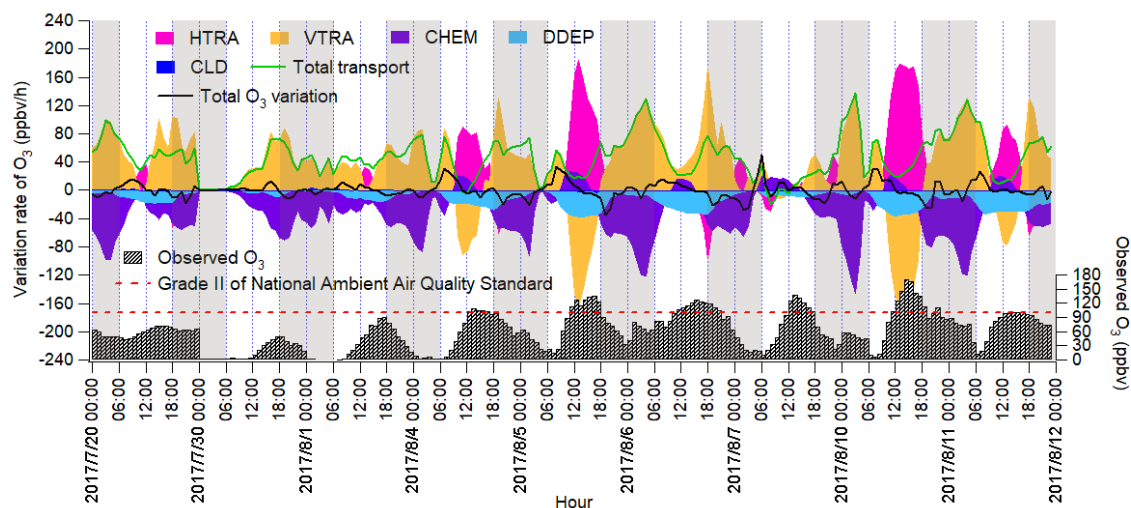


Figure 6 Time series of O₃ variation rate in Ji'nan induced by individual processes calculated based on the change of O₃ per hour. Total transport is the sum of HTRA and VTRA, and the sum of O₃ variation rates attributable to all the processes is represented by total O₃ variation rate. The nighttime (18:00 – 06:00 LT) has been highlighted in grey.

3.4 Local O₃ formation and control

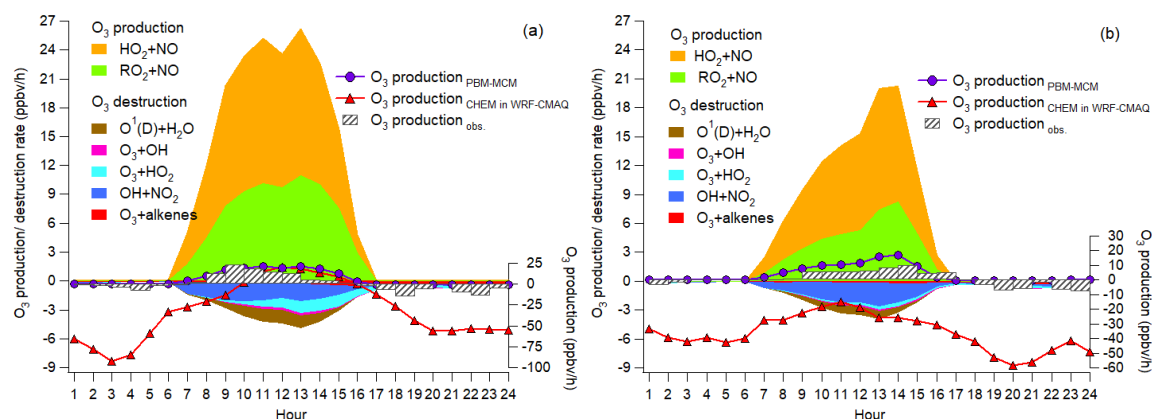
3.4.1 Pathway and source contributions to O₃ production

The IPR analyses showed that chemical reactions served as an important source of O₃ on episode days in Ji'nan, particularly during 09:00-15:00 LT when O₃ was at high levels. This process was further studied through the simulation of the in-situ photochemistry by PBM-MCM. It should be noted that the simulations were based on the observed concentrations of O₃ precursors, which could be influenced by both local and regional air. It required cautions to extend the results to all the situations in Ji'nan, because the regional effect was not always consistent. Table S5 lists the production and destruction pathways of O₃ (Thornton et al., 2002; Monks, 2005; Kanaya et al., 2009). Briefly, the oxidation of NO by HO₂ and RO₂ produced NO₂, which led to O₃ formation following NO₂ photolysis (R2 and R4-R5 in introduction). Therefore, the reactions between NO and HO₂/RO₂ were considered as the production pathways of O₃. To account for O₃ destruction, reaction between O¹(D) and H₂O denoted the photolysis of O₃, and reactions of O₃ with OH, HO₂ and alkenes were also included. Furthermore, since HNO₃ was an important sink of NO₂, the reaction between OH and NO₂ was treated to be destructive to O₃. The titration of O₃ by NO was not included in O₃ destruction, because NO₂ produced in this reaction was either not considered as a source of O₃.

Figure 7 (a) and (b) show the 24 hour average simulated pathway contributions to O₃ production rate for the 6 O₃ episode days and 3 non-episode days. Also shown are the O₃ production rates simulated by PBM-MCM (O₃ production_{PBM-MCM}), those simulated by WRF-CMAQ simulation (O₃ production_{CHEM}), and those calculated from the observed hourly O₃ (O₃ production_{obs.}). Overall, O₃ production_{PBM-MCM} and O₃ production_{obs.} were on the same magnitudes, especially during O₃ episodes with more stagnant weather conditions. This indicated that the PBM-MCM model reasonably reproduced the in situ O₃ photochemistry. Though obvious discrepancies existed between O₃ production_{CHEM} and O₃ production_{PBM-MCM}, they agreed well with each other during 10:00-15:00 LT on episode days, consistent with the finding that chemical reactions made great contributions to O₃ in this period (Figure 6). The lower or even negative O₃ production_{CHEM} resulted from the titration of the regionally transported and/or local background O₃ by NO and the following depletion of NO₂ through reacting with OH and/or transport. Differently, PBM-MCM did not consider the transport of O₃, though the transport effect was partially represented by constraining the model to the observed concentrations of O₃ precursors. In addition, the PBM-MCM was constructed by the observed air pollutants, which were already subject to chemical reactions before being detected by the analytical instruments. This meant that

the reaction between NO and O₃ from the emission to the detection of NO_x was not considered in PBM-MCM. However, as an emission-based model, WRF-CMAQ performed better in describing the reactions immediately after the emissions of air pollutants. Therefore, the chemical destructions of O₃ in the vicinity of NO_x sources also accounted for the aforementioned discrepancy. The obviously higher reaction rate between NO and O₃ simulated by WRF-CMAQ (Figure S12) confirmed our inferences.

During both O₃ episodes and non-episodes, the reaction between HO₂ and NO dominated over “RO₂+NO” in O₃ production, while the O₃ destruction was mainly attributable to the formation of HNO₃, the reaction between O₃ and HO₂ and photolysis of O₃. The net O₃ production rate during O₃ episodes (maximum: 21.3 ppbv/hr) was much ($p<0.05$) higher than during non-episodes (maximum: 16.9 ppbv/hr), which partially explained the higher O₃ on episode days. In general, “OH+NO₂” serves as the chain terminating reaction in VOC-limited regime of O₃ formation, while the radical-radical reactions take over the role in NO_x-limited regime (Finlayson-Pitts and Pitts, 1993; Kleinman, 2005). Here, we found that the ratio of total reaction rates between “HO₂+RO₂” and “OH+NO₂” substantially increased from 0.2±0.1 during non-episodes to 1.0±0.3 during O₃ episodes ($p<0.05$). This suggested that O₃ formation during non-episodes was limited by VOCs, while it switched to be co-limited by VOCs and NO_x during O₃ episodes in view of the equivalent role of “HO₂+RO₂” and “OH+NO₂” in terminating the chain reactions.



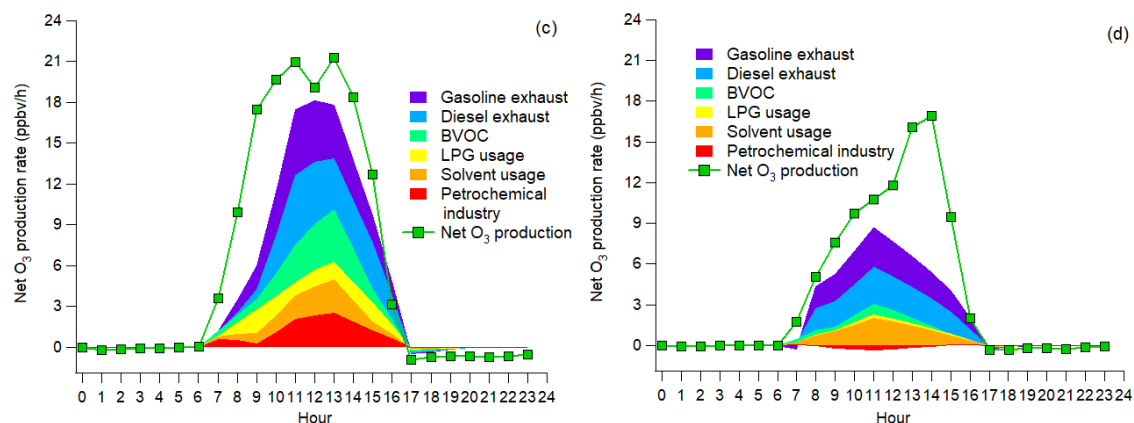


Figure 7 Pathway contributions to O₃ production and destruction rate during episodes (a) and non-episodes (b). Contributions of O₃ precursor sources to net O₃ production rate during episodes (c) and non-episodes (d).

Further, the 24 hour average contributions to net O₃ production rate of different sources of O₃ precursors were identified for the 6 episode days and 3 non-episode days, as presented in Figure 7 (c) and (d). Text S2 and Figure S13 illustrate the source apportionment of O₃ precursors and the simulations of the source-specific contributions to O₃ production rates. The results are presented in Table 2. Since the source apportionment was performed for the ambient O₃ precursors which were already subject to atmospheric processes, such as dispersion, deposition and chemical reactions, the results represented the source contributions to the steady – state concentrations of O₃ precursors and the corresponding O₃ productions. It was found that gasoline exhaust and diesel exhaust were the largest contributors to O₃ production regardless of O₃ episodes or non-episodes. Specifically, the net O₃ production rate was 1.0 ± 0.3 ppbv/hr for both gasoline and diesel exhaust during non-episodes, which however increased to 1.8 ± 0.6 ppbv/hr for gasoline exhaust and 1.7 ± 0.4 ppbv/hr for diesel exhaust during O₃ episodes. This suggested that vehicular emissions played critical roles in building up ground-level O₃ in Ji'nan. If carbonyls were taken into account, the contributions of vehicular emissions to O₃ production rate were even higher than the currently simulated values, due to the dominance of vehicular exhausts in the sources of carbonyls in urban areas (Grosjean et al., 1990; Granby et al., 1997). In addition, the contributions of the other sources to O₃ production rates all increased during O₃ episodes except for solvent usage ($p > 0.05$), as listed in Table 2. It is not surprising to see the coincident increases, in view of the higher simulated and observed overall O₃ production rate during episodes.

Further insight into the percentage contributions (not shown here) found that the contributions of BVOC, LPG usage and petrochemical industry relative to the sum of the O₃ production rates of the 6 sources increased substantially from 9.9±4.2%, 4.3±1.4% and -2.8±1.9% during non-episodes to 19.2±4.3%, 9.1±3.4% and 12.1±3.1% during O₃ episodes, respectively. The increased O₃ production rates by BVOCs could be explained by the increase of isoprene (episodes: 2.2±0.6 ppbv; non-episodes: 0.9±0.3 ppbv), under higher temperature and stronger solar radiation during O₃ episodes. The enhanced O₃ formation from petrochemical industry on episode days was likely associated with the dominance of continental air (Figure 4) and the extensive petrochemical industries in the NCP. For example, the mixing ratio of styrene increased from 54.7±22.0 pptv during non-episodes to 162.3±44.7 pptv during O₃ episodes. The reason for elevated O₃ production rate by LPG usage during episodes was unknown. It is worth noting that the source contributions to O₃ production might have some uncertainty due to the limited number of samples (54 samples) and O₃ precursors (31 VOCs, CO, NO and NO₂) for source apportionment.

Table 2 Contributions to VOCs, CO, NO, NO₂ and O₃ production rate by the sources of O₃ precursors averaged on the VOC sampling days in Ji'nan (Unit: % unless otherwise specified).

Source	VOCs*	CO	NO	NO ₂	O ₃ production rate (ppbv/hr)	
					O ₃ episodes	Non-episodes
GE ¹	25.7±3.6	29.9±2.1	30.9±2.4	22.2±2.4	1.8±0.6	1.0±0.3
DE ²	17.6±2.4	57.3±5.2	52.0±5.8	54.4±5.8	1.7±0.4	1.0±0.3
BVOC	6.1±2.6	0.0±1.7	0.0±2.8	0.0±2.3	1.2±0.5	0.2±0.1
LPG ³	14.7±2.0	2.2±1.1	9.1±1.6	4.7±0.9	0.8±0.5	0.1±0.1
Solvent ⁴	17.1±3.9	3.1±1.8	5.1±3.8	7.8±3.1	0.8±0.5	0.7±0.3
PI ⁵	18.8±3.1	7.4±1.9	2.9±1.8	10.9±2.5	1.0±0.3	-0.1±0.1

VOCs*: VOCs applied in source apportionment (see Text S2).

¹ gasoline exhaust, ² diesel exhaust, ³ LPG usage, ⁴ solvent usage and ⁵ petrochemical industry.

3.4.2 O₃ control measures

Both WRF-CMAQ and PBM-MCM revealed the significant local O₃ production in the O₃ pollution event. The relationships between O₃ and its precursors need to be clarified, so that the science-based control measures can be taken. Throughout the VOC sampling period, the OH

reactivity of VOCs ($OH\ reactivity_{VOCs}$) were within the range of 33-123% of the average $OH\ reactivity_{VOCs}$ during O_3 episodes. For OH reactivity of NO_x ($OH\ reactivity_{NOx}$), the range was 61-242%. The O_3 production rates were simulated in a set of assumed scenarios with different $OH\ reactivity_{VOCs}$ and $OH\ reactivity_{NOx}$. To include the OH reactivity of VOCs and NO_x on all the VOC sampling days, factors from 10% to 140% with the step of 10% were applied to the average diurnal profiles of VOCs and CO during O_3 episodes, while the factors ranged from 10% to 300% with the step of 10% for NO_x . The initial concentrations of all the air pollutants were also scaled by the factors and the model was constrained to these scaled concentrations every hour, except for O_3 . It should be noted that the factors applied to CO were exactly the same as those applied to VOCs, therefore we use $VOCs^\#$ to represent the sum of VOCs and CO hereafter. The 14 gradients of $OH\ reactivity_{VOCs^\#}$ and 30 gradients of $OH\ reactivity_{NOx}$ made up 420 scenarios. Meteorological conditions were exactly the same for all the scenarios and the clear sky was hypothesized. According to the simulations, the maximums of the O_3 production rates occurred at 12:00 LT. Thus, the simulated O_3 production rates at 12:00 LT, as a function of $OH\ reactivity_{VOCs}$ and $OH\ reactivity_{NOx}$, are plotted in Figure 8. Text S3 describes the methods to define the regimes controlling O_3 formation.

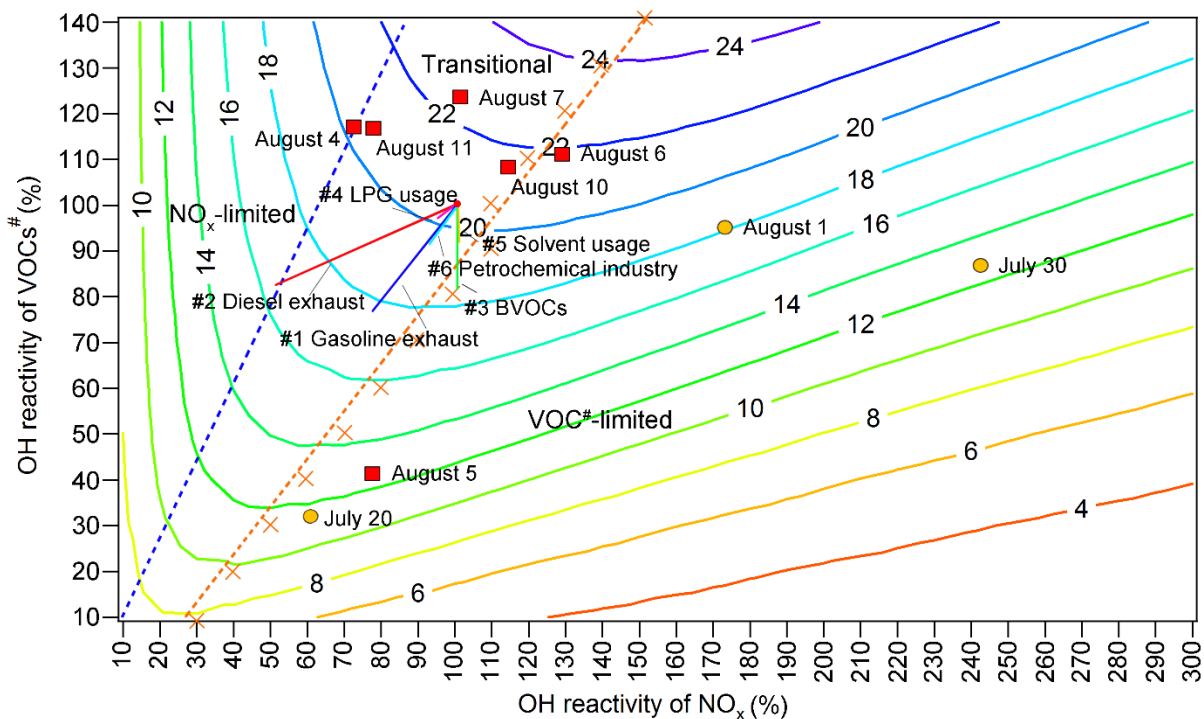


Figure 8 Isopleths of the net O₃ production rate (ppbv/hr) at 12:00 LT as a function of $OH\ reactivity_{VOCs^{\#}}$ and $OH\ reactivity_{NOx}$. The red blocks and orange circles denote the calculated $OH\ reactivity_{VOCs^{\#}}$ and $OH\ reactivity_{NOx}$ at 12:00 LT on O₃ episode and non-episode days, respectively. Each orange cross represents the $OH\ reactivity_{VOCs^{\#}}$ and $OH\ reactivity_{NOx}$ at 12:00 LT in the scenario with highest O₃ production rate at a given $OH\ reactivity_{VOCs^{\#}}$. The orange dashed line and blue dashed line divide O₃ formation into the VOC-limited regime, transitional regime, and NO_x-limited regime.

It was found that O₃ formation was mainly limited by VOCs[#] during non-episodes. However, it switched to be co-limited by VOCs[#] and NO_x (transitional regime) on episode days with the net O₃ production rate among the highest, except for August 5 when the strong sea breeze diluted air pollutants in Ji'nan and/or intercept the transport of air pollutants from Central China to Ji'nan (Figure S6). In reality, the sensitivity of O₃ formation to NO_x might be underemphasized due to the positive biases of NO₂ measurement (Lu et al., 2010). This effect was expected to be more significant during episodes when the overestimates of NO₂ were higher. However, O₃ formation was not likely only limited by NO_x even during O₃ episodes, which should be still sensitive to VOCs, as NO₂ could not be much overestimated in the urban areas (see section 2.2.1). Therefore, O₃ formation was considered to be in the transitional regime during episodes. This partially explained the increased O₃ during episodes in Ji'nan, given the higher O₃ production rates in transitional regime (Figure 8). Noticeably, the change of regimes controlling O₃ formation is consistent with that predicted by the $\frac{OH\ reactivity_{VOCs^{\#}}}{OH\ reactivity_{NOx}}$ ratio and the ratio of the reaction rates between “HO₂+RO₂” and “OH+NO₂”.

The source apportionment of O₃ precursors enabled us to calculate the source-specific $OH\ reactivity_{VOCs^{\#}}$ and $OH\ reactivity_{NOx}$. Accordingly, the variations of O₃ production rates induced by the reductions in source emissions are presented in Figure 8 (straight solid lines #1-#6). The start point of the straight lines corresponded to 100% of the total average $OH\ reactivity_{VOCs^{\#}}$ and $OH\ reactivity_{NOx}$ during O₃ episodes. The end points, however, denoted the $OH\ reactivity_{VOCs^{\#}}$ and $OH\ reactivity_{NOx}$ with the complete elimination of emissions from the individual sources. Therefore, the differences of the O₃ production rate between the start point and end points were the source contributions to the O₃ production rate,

while the lengths of the lines reflected the contributions to the OH reactivity. Further, the simulated O₃ production rates on the lines #1-#6, as a response of reductions in source emissions, are extracted and plotted in Figure S14. Obviously, the highest efficiencies of O₃ reduction could be achieved by cutting diesel exhaust (0.58 ppbv hr⁻¹/10% emission reduction) and gasoline exhaust (0.47 ppbv hr⁻¹/10% emission reduction). In fact, the sensitivity of O₃ production rate to the vehicle exhausts might be somewhat underestimated, due to the exclusion of carbonyls in the source apportionment. However, the reductions of O₃ production rate by cutting 10% of vehicle exhausts were still insignificant, compared to the overall maximum O₃ production rate of 21.3 ppbv/hr during O₃ episodes. This indicated that by only restraining emissions from one to two sources, high percentages of emission reductions were required to sufficiently reduce the O₃ production rate. Otherwise, the combined efforts should be made to control the emissions of O₃ precursors from the diverse sources. In particular, it is essential to get rid of the transitional regime featuring high O₃ production rates and low sensitivities of O₃ production to the precursors.

4 Implications

This study investigates the causes of a severe O₃ pollution event lasting for eight consecutive days in the NCP, one of the most densely populated regions in the world. Photochemical O₃ formation in the lower troposphere of the NCP is demonstrated as the main source, under the synoptic conditions of weak high pressure or low pressure trough. Though NO_x, as an important precursor of O₃, has been significantly reduced in emissions in China since 2013 (Duncan et al., 2016; Liu et al., 2017), O₃ pollution is still severe or even becoming worse in the NCP, as revealed in the present and also previous studies (Zhang et al., 2014; Sun et al., 2016). The finding that O₃ formation shifted from VOC-limited regime on relatively low O₃ days to the transitional regime on O₃ non-attainment days may elucidate the cause of the increase in O₃, because O₃ productions in the transitional regime are even higher, despite decreases in NO_x emissions. It is unrealistic to expect a continuously linear reduction in NO_x emissions in the NCP, after the substantial decreases of NO_x emissions from power plants and industries in recent years. In other words, restraining on VOC emissions is urgent for O₃ abatement in the NCP. Another important finding in this study was that the NCP served as an O₃ source. This was ever proposed by Ding et al. (2009), based on the aircraft measurement and simulation of atmospheric dynamics. We confirmed it through the ground-level observation and the simulation of in-situ

photochemistry. It can be expected that organic nitrates are also intensively formed in the NCP as byproducts in the photochemical cycles of O₃ formation. In combination with the fact that the NCP locates within the mid-latitude band of Northern Hemisphere under the dominance of westerlies, O₃ and organic nitrates formed in this region can be transported over a long distance following uplift processes, which has been confirmed to partially account for the enhancement of background O₃ in North America and even Europe (Derwent et al., 2015; Lin et al., 2017). Therefore, the recent air pollution control measures taken in China (including China's Clean Air Act Plan in force in 2013) are still inadequate to ease the global O₃ burden in a short period. More effective Action Plans should be implemented to achieve an O₃ benefit, with comprehensive thinking of atmospheric dynamics and chemistry.

Acknowledgements: This study was supported by the National Key R&D Program of China (2017YFC0212001), the Research Grants Council of the Hong Kong Special Administrative Region via grants PolyU5154/13E, PolyU152052/14E, PolyU152052/16E, CRF/C5004-15E and CRF/C5022-14G, the Collaborative Research program between The Beijing University of Technology and The Hong Kong Polytechnic University (PolyU) (4-ZZFW), the Hong Kong Polytechnic University PhD scholarships (project RTUP), and the National Natural Science Foundation of China (No. 41675118). This study is partly supported by the Hong Kong PolyU internal grant (G-YBUQ, 1-ZVJT and 1-BBW4). The data are accessible at https://drive.google.com/open?id=1_KeOxOuVsLY83xL74RtcRORSiiyIR8FZ.

References

- Atkinson, R.: Atmospheric chemistry of VOCs and NO_x, *Atmos. Environ.*, 34, 2063-2101, **2000**.
- Beck, J.P. and Grennfelt, P.: Estimate of ozone production and destruction over northwestern Europe, *Atmos. Environ.*, 28, 129-140, **1994**.
- Cai, C., Geng, F., Tie, X., Yu, Q., and An, J.: Characteristics and source apportionment of VOCs measured in Shanghai, China, *Atmos. Environ.*, 44, 5005-5014, **2010**.
- Carter, W.P.: Development of ozone reactivity scales for volatile organic compounds, *Air & Waste Manage. Assoc.*, 44, 881-899, **1994**.

693 Carter, W.P., Pierce, J.A., Luo, D., and Malkina, I.L.: Environmental chamber study of
 694 maximum incremental reactivities of volatile organic compounds, *Atmos. Environ.*, 29(18),
 695 2499-2511, **1995**.

696 Chameides, W. and Walker, J.C.: A photochemical theory of tropospheric ozone, *J. Geophys.*
 697 *Res.*, 78(36), 8751-8760, **1973**.

698 Chan, C.Y. and Chan, L.Y.: Effect of meteorology and air pollutant transport on ozone episodes
 699 at a subtropical coastal Asian city, Hong Kong, *J. Geophys. Res. – Atmos.*, 105(D16), 20707-
 700 20724, **2000**.

701 Chen, Y., Zhao, C., Zhang, Q., Deng, Z., Huang, M., and Ma, X.: Aircraft study of mountain
 702 chimney effect of Beijing, China, *J. Geophys. Res. – Atmos.*, 114(D8),
 703 doi:10.1029/2008JD010610, **2009**.

704 Cheng, H., Guo, H., Wang, X., Saunders, S.M., Lam, S.H.M., Jiang, F., Wang, T., Ding, A., Lee,
 705 S., and Ho, K.F.: On the relationship between ozone and its precursors in the Pearl River Delta:
 706 application of an observation-based model (OBM), *Environ. Sci. Pollut. Res.*, 17(3), 547-560,
 707 **2010**.

708 Colman, J.J., Swanson, A.L., Meinardi, S., Sive, B.C., Blake, D.R., and Rowland, F.S.:
 709 Description of the analysis of a wide range of volatile organic compounds in whole air samples
 710 collected during PEM-Tropics A and B, *Anal. Chem.*, 73(15), 3723-3731, **2001**.

711 Cooper, O.R., Stohl, A., Hübner, G., Hsie, E.Y., Parrish, D.D., Tuck, A.F., Kiladis, G.N.,
 712 Oltmans, S.J., Johnson, B.J., Shapiro, M., and Moody, J.L.: Direct transport of midlatitude
 713 stratospheric ozone into the lower troposphere and marine boundary layer of the tropical Pacific
 714 Ocean, *J. Geophys. Res.: Atmos.*, 110(D23), **2005**.

715 Crutzen, P.: A discussion of the chemistry of some minor constituents in the stratosphere and
 716 troposphere, *Pure Appl. Geophys.*, 106(1), 1385-1399, **1973**.

717 Derwent, R.G., Utembe, S.R., Jenkin, M.E., and Shallcross, D.E.: Tropospheric ozone
 718 production regions and the intercontinental origins of surface ozone over Europe, *Atmos.*
 719 *Environ.*, 112, 216-224, **2015**.

720 Ding, A.J., Fu, C.B., Yang, X.Q., Sun, J.N., Zheng, L.F., Xie, Y.N., Herrmann, E., Nie, W.,
 721 Petaja, T., Kerminen, V.M., and Kulmala, M.: Ozone and fine particle in the western Yangtze
 722 River Delta: an overview of 1 yr data at the SORPES station, *Atmos. Chem. Phys.*, 13(11):5813-
 723 30, **2013**.

724 Ding, A., Wang, T., Xue, L., Gao, J., Stohl, A., Lei, H., Jin, D., Ren, Y., Wang, X., Wei, X., and
 725 Qi, Y.: Transport of north China air pollution by midlatitude cyclones: Case study of aircraft
 726 measurements in summer 2007, *J. Geophys. Res.: Atmos.*, 114(D8), **2009**.

727 Duncan, B.N., Lamsal, L.N., Thompson, A.M., Yoshida, Y., Lu, Z., Streets, D.G., Hurwitz,
 728 M.M., and Pickering, K.E.: A space-based, high-resolution view of notable changes in urban
 729 NO_x pollution around the world (2005-2014), *J. Geophys. Res.: Atmos.*, 121(2), 976-996, **2016**.

730 Dunlea, E.J., Herndon, S.C., Nelson, D.D., Volkamer, R.M., San Martini, F., Sheehy, P.M.,
 731 Zahniser, M.S., Shorter, J.H., Wormhoudt, J.C., Lamb, B.K., and Allwine, E.J.: Evaluation of
 732 nitrogen dioxide chemiluminescence monitors in a polluted urban environment, *Atmos. Chem.*
 733 *Phys.*, 7(10), 2691-2704, **2007**.

734 Finlayson-Pitts, B.J., and Pitts Jr, J.N.: Atmospheric chemistry of tropospheric ozone formation:
 735 scientific and regulatory implications, *Air & Waste Manage. Assoc.*, 43(8), 1091-1100, **1993**.

736 Fung, J.C.H., Lau, A.K.H., Lam, J.S.L., and Yuan, Z.: Observational and modeling analysis of a
 737 severe air pollution episode in western Hong Kong, *J. Geophys. Res. – Atmos.*, 110(D9), **2005**.

738 Gao, J., Wang, T., Ding, A., and Liu, C.: Observational study of ozone and carbon monoxide at
 739 the summit of mount Tai (1534m asl) in central-eastern China, *Atmos. Environ.*, 39(26), 4779-
 740 4791, **2005**.

741 Granby, K., Christensen, C.S., and Lohse, C.: Urban and semi-rural observations of carboxylic
 742 acids and carbonyls, *Atmos. Environ.*, 31(10), 1403-1415, **1997**.

743 Grosjean, D., Miguel, A.H., and Tavares, T.M.: Urban air pollution in Brazil: Acetaldehyde and
 744 other carbonyls, *Atmos. Environ.*, 24(1), 101-106, **1990**.

745 Gu, D., Wang, Y., Smeltzer, C., and Boersma, K.F.: Anthropogenic emissions of NO_x over
 746 China: Reconciling the difference of inverse modeling results using GOME-2 and OMI
 747 measurements. *J. Geophys. Res.: Atmos.*, 119(12):7732-40, **2014**.

748 Guo, H., Ling, Z.H., Cheung, K., Jiang, F., Wang, D.W., Simpson, I.J., Barletta, B., Meinardi, S.,
 749 Wang, T.J., Wang, X.M., Saunders, S.M., and Blake, D.R.: Characterization of photochemical
 750 pollution at different elevations in mountainous areas in Hong Kong, *Atmos. Chem. Phys.*, 13(8),
 751 3881-3898, **2013**.

752 Han, X., Zhu, L., Wang, S., Meng, X., Zhang, M., and Hu, J.: Modeling study of impacts on
 753 surface ozone of regional transport and emissions reductions over North China Plain in summer
 754 2015, *Atmos. Chem. Phys.*, 18(16):12207-21, **2018**.

755 He, J., Wang, Y., Hao, J., Shen, L., and Wang, L.: Variations of surface O₃ in August at a rural
 756 site near Shanghai: influences from the West Pacific subtropical high and anthropogenic
 757 emissions, *Environ. Sci. Pollut. Res.*, 19(9), 4016-4029, **2012**.

758 He, K.: Multi-resolution Emission Inventory for China (MEIC): model framework and 1990-
 759 2010 anthropogenic emissions, In AGU Fall Meeting Abstracts, December, **2012**.

760 Huang, J.P., Fung, J.C., Lau, A.K., and Qin, Y.: Numerical simulation and process analysis of
 761 typhoon-related ozone episodes in Hong Kong, *J. Geophys. Res. – Atmos.*, 110(D5), **2005**.

762 Jenkin, M.E. and Clemitshaw, K.C.: Ozone and other secondary photochemical pollutants:
 763 chemical processes governing their formation in the planetary boundary layer, *Atmos. Environ.*,
 764 34(16), 2499-2527, **2000**.

765 Jenkin, M.E., Saunders, S.M., and Pilling, M.J.: The tropospheric degradation of volatile organic
 766 compounds: a protocol for mechanism development, *Atmos. Environ.*, 31(1), 81-104, **1997**.

767 Jiang, F., Guo, H., Wang, T.J., Cheng, H.R., Wang, X.M., Simpson, I.J., Ding, A.J., Saunders,
 768 S.M., Lam, S.H.M., and Blake, D.R.: An ozone episode in the Pearl River Delta: Field
 769 observation and model simulation, *J. Geophys. Res. – Atmos.*, 115(D22), **2010**.

770 Jin, X., Fiore, A.M., Murray, L.T., Valin, L.C., Lamsal, L.N., Duncan, B., Folkert Boersma, K.,
 771 De Smedt, I., Abad, G.G., Chance, K., and Tonnesen, G.S.: Evaluating a Space-Based Indicator
 772 of Surface Ozone-NO_x-VOC Sensitivity Over Midlatitude Source Regions and Application to
 773 Decadal Trends, *J. Geophys. Res.: Atmos.*, 122(19), **2017**.

774 Kanaya, Y., Pochanart, P., Liu, Y., Li, J., Tanimoto, H., Kato, S., Suthawaree, J., Inomata, S.,
 775 Taketani, F., Okuzawa, K., and Kawamura, K.: Rates and regimes of photochemical ozone

776 production over Central East China in June 2006: a box model analysis using comprehensive
 777 measurements of ozone precursors, *Atmos. Chem. Phys.*, 9(20), 7711-7723, **2009**.

778 Kleinman, L.I.: The dependence of tropospheric ozone production rate on ozone precursors,
 779 *Atmos. Environ.*, (3), 575-586, **2005**.

780 Kusaka, H. and Kimura, F.: Coupling a single-layer urban canopy model with a simple
 781 atmospheric model: Impact on urban heat island simulation for an idealized case, *J. Meteorol. Soc.*
 782 *Japan: Ser. II*, 82(1), 67-80, **2004**.

783 Lam, S.H.M., Saunders, S.M., Guo, H., Ling, Z.H., Jiang, F., Wang, X.M., and Wang, T.J.:
 784 Modelling VOC source impacts on high ozone episode days observed at a mountain summit in
 785 Hong Kong under the influence of mountain-valley breezes, *Atmos. Environ.*, 81, 166-176, **2013**.

786 Lang, J., Zhang, Y., Zhou, Y., Cheng, S., Chen, D., Guo, X., Chen, S., Li, X., Xing, X., and
 787 Wang, H.: Trends of PM_{2.5} and chemical composition in Beijing, 2000–2015, *Aerosol Air Qual.*
 788 *Res.*, 17, 412-425, **2017**.

789 Li, M., Zhang, Q., Kurokawa, J.I., Woo, J.H., He, K., Lu, Z., Ohara, T., Song, Y., Streets, D.G.,
 790 Carmichael, G.R., and Cheng, Y.: MIX: a mosaic Asian anthropogenic emission inventory under
 791 the international collaboration framework of the MICS-Asia and HTAP, *Atmos. Chem. Phys.*,
 792 17(2), **2017**.

793 Lin, M., Fiore, A.M., Horowitz, L.W., Langford, A.O., Oltmans, S.J., Tarasick, D., and Rieder,
 794 H.E.: Climate variability modulates western US ozone air quality in spring via deep stratospheric
 795 intrusions, *Nat. Commun.*, 6:7105, **2015**.

796 Lin, M., Horowitz, L.W., Payton, R., Fiore, A.M., and Tonnesen, G.: US surface ozone trends
 797 and extremes from 1980 to 2014: quantifying the roles of rising Asian emissions, domestic
 798 controls, wildfires, and climate, *Atmos. Chem. Phys.*, 17(4), 2943-2970, **2017**.

799 Lin, W., Xu, X., Zhang, X., and Tang, J.: Contributions of pollutants from North China Plain to
 800 surface ozone at the Shangdianzi GAW Station, *Atmos. Chem. Phys.*, 8(19), 5889-5898, **2008**.

801 Liu, F., Beirle, S., Zhang, Q., Zheng, B., Tong, D., and He, K.: NO_x emission trends over
 802 Chinese cities estimated from OMI observations during 2005 to 2015, *Atmospheric chemistry*
 803 *and physics*, 17(15), 9261-9275, **2017**.

804 Liu, X.H., Zhang, Y., Xing, J., Zhang, Q., Wang, K., Streets, D.G., Jang, C., Wang, W.X., and
805 Hao, J.M.: Understanding of regional air pollution over China using CMAQ, part II. Process
806 analysis and sensitivity of ozone and particulate matter to precursor emissions, *Atmos. Environ.*,
807 44(30), 3719-3727, **2010**.

808 Lo, J.C., Lau, A.K., Fung, J.C., and Chen, F.: Investigation of enhanced cross-city transport and
809 trapping of air pollutants by coastal and urban land-sea breeze circulations, *J. Geophys. Res. –*
810 *Atmos.*, 111(D14), **2006**.

811 Lyu, X.P., Chen, N., Guo, H., Zhang, W.H., Wang, N., Wang, Y., and Liu, M.: Ambient volatile
812 organic compounds and their effect on ozone production in Wuhan, central China, *Sci. Total*
813 *Environ.*, 541:200-9, **2016**.

814 Lyu, X.P., Guo, H., Wang, N., Simpson, I.J., Cheng, H.R., Zeng, L.W., Saunders, S.M., Lam, S.
815 H.M., Meinardi, S., and Blake, D.R.: Modeling C₁-C₄ alkyl nitrate photochemistry and their
816 impacts on O₃ production in urban and suburban environments of Hong Kong, *J. Geophys. Res.*
817 *– Atmos.*, 122(19), **2017**.

818 Lu, K., Zhang, Y., Su, H., Brauers, T., Chou, C.C., Hofzumahaus, A., Liu, S.C., Kita, K., Kondo,
819 Y., Shao, M., and Wahner, A.: Oxidant (O₃ + NO₂) production processes and formation regimes
820 in Beijing, *J. Geophys. Res.: Atmos.*, 115(D7), **2010**.

821 Madronich, S. and Flocke, S.: Theoretical estimation of biologically effective UV radiation at the
822 Earth's surface, In *Solar Ultraviolet Radiation* (pp. 23-48), Springer, Berlin, Heidelberg, **1997**.

823 Mao, J., Ren, X., Chen, S., Brune, W.H., Chen, Z., Martinez, M., Harder, H., Lefer, B.,
824 Rappenglueck, B., Flynn, J., and Leuchner, M.: Atmospheric oxidation capacity in the summer
825 of Houston 2006: Comparison with summer measurements in other metropolitan studies, *Atmos.*
826 *Environ.*, 44(33), 4107-4115, **2010**.

827 McClenny, W.A., Williams, E.J., Cohen, R.C., and Stutz, J.: Preparing to measure the effects of
828 the NO_x SIP Call—methods for ambient air monitoring of NO, NO₂, NO_y, and individual NO_z
829 species, *Air & Waste Manage. Assoc.*, 52(5), 542-562, **2002**.

830 Monks, P. S.: Gas-phase radical chemistry in the troposphere, *Chem. Soc. Reviews*, 34(5), 376-
831 395, **2005**.

Ren, X., Harder, H., Martinez, M., Leshner, R.L., Oliger, A., Simpao, J.B., Brune, W.H., Schwab, J.J., Demerjian, K.L., He, Y., and Zhou, X.: OH and HO₂ chemistry in the urban atmosphere of New York City, *Atmos. Environ.*, 37(26), 3639-3651, **2003**.

Saunders, S.M. Jenkin, M.E., Derwent, R.G., and Pilling, M.J.: Protocol for the development of the Master Chemical Mechanism, MCM v3 (Part A): tropospheric degradation of non-aromatic volatile organic compounds, *Atmos. Chem. Phys.*, 3(1), 161-180, **2003**.

Shan, W., Yin, Y., Zhang, J., and Ding, Y.: Observational study of surface ozone at an urban site in East China, *Atmos. Res.*, 89(3), 252-261, **2008**.

Shao, M., Lu, S., Liu, Y., Xie, X., Chang, C., Huang, S., and Chen, Z.: Volatile organic compounds measured in summer in Beijing and their role in ground-level ozone formation, *J. Geophys. Res. – Atmos.*, 114(D2), doi.org/10.1029/2008JD010863, **2009b**.

Shu, L., Xie, M., Wang, T., Gao, D., Chen, P., Han, Y., Li, S., Zhuang, B., and Li, M.: Integrated studies of a regional ozone pollution synthetically affected by subtropical high and typhoon system in the Yangtze River Delta region, China, *Atmos. Chem. Phys.*, 16(24), 15801-15819, **2016**.

Sillman, S.: The relation between ozone, NO_x and hydrocarbons in urban and polluted rural environments, *Atmos. Environ.*, 33(12), 1821-1845, **1999**.

Sun, L., Xue, L., Wang, T., Gao, J., Ding, A., Cooper, O.R., Lin, M., Xu, P., Wang, Z., Wang, X., Wen, L., Zhu, Y., Chen, T., Yang, L., Wang, Y., Chen, J., and Wang, W.: Significant increase of summertime ozone at Mount Tai in Central Eastern China, *Atmos. Chem. Phys.*, 16(16), 10637-10650, **2016**.

Tan, Z., Lu, K., Dong, H., Hu, M., Li, X., Liu, Y., Lu, S., Shao, M., Su, R., Wang, H., and Wu, Y.: Explicit diagnosis of the local ozone production rate and the ozone-NO_x-VOC sensitivities, *Sci. Bull.*, 63(16):1067-76, **2018**.

Tan, Z., Lu, K., Jiang, M., Su, R., Dong, H., Zeng, L., Xie, S., Tan, Q., and Zhang, Y.: Exploring ozone pollution in Chengdu, southwestern China: A case study from radical chemistry to O₃-VOC-NO_x sensitivity, *Sci. Total Environ.*, 636:775-86, **2018**.

Thornton, J.A., Wooldridge, P.J., Cohen, R.C., Martinez, M., Harder, H., Brune, W.H., Williams, E.J., Roberts, J.M., Fehsenfeld, F.C., Hall, S.R., and Shetter, R.E.: Ozone production rates as a

861 function of NO_x abundances and HO_x production rates in the Nashville urban plume, J. Geophys.
862 Res. – Atmos., 107(D12), doi.org/10.1029/2001JD000932, **2002**.

863 Wang, N., Guo, H., Jiang, F., Ling, Z. H., and Wang, T.: Simulation of ozone formation at
864 different elevations in mountainous area of Hong Kong using WRF-CMAQ model, Sci. Total
865 Environ., 505, 939-951, **2015b**.

866 Wang, T., Ding, A., Gao, J., and Wu, W.S.: Strong ozone production in urban plumes from
867 Beijing, China, Geophys. Res. Lett., 33(21), **2006**.

868 Wang, T., Nie, W., Gao, J., Xue, L.K., Gao, X.M., Wang, X.F., Qiu, J., Poon, C.N., Meinardi, S.,
869 Blake, D., Wang, S.L., Ding, A.J., Chai, F.H., Zhang, Q.Z., and Wang, W.X.: Air quality during
870 the 2008 Beijing Olympics: secondary pollutants and regional impact, Atmos. Chem. Phys.,
871 10(16), 7603-7615, **2010**.

872 Wang, X.M., Lin, W.S., Yang, L.M., Deng, R.R., and Lin, H.: A numerical study of influences
873 of urban land - use change on ozone distribution over the Pearl River Delta region, China, Tellus
874 B, 59(3), 633-641, **2007**.

875 Wang, Z., Li, Y., Chen, T., Zhang, D., Sun, F., Wei, Q., Dong, X., Sun, R., Huan, N., and Pan, L.:
876 Ground-level ozone in urban Beijing over a 1-year period: Temporal variations and relationship
877 to atmospheric oxidation, Atmos. Res., 164, 110-117, **2015a**.

878 Whitten, G.Z., Heo, G., Kimura, Y., McDonald-Buller, E., Allen, D.T., Carter, W.P., and
879 Yarwood, G.: A new condensed toluene mechanism for Carbon Bond: CB05-TU, Atmos.
880 Environ., 44(40), 5346-5355, **2010**.

881 Williams, J., Keßel, S.U., Nölscher, A.C., Yang, Y., Lee, Y., Yáñez-Serrano, A.M., Wolff, S.,
882 Kesselmeier, J., Klüpfel, T., Lelieveld, J., and Shao, M.: Opposite OH reactivity and ozone
883 cycles in the Amazon rainforest and megacity Beijing: Subversion of biospheric oxidant control
884 by anthropogenic emissions, Atmos. Environ., 125, 112-118, **2016**.

885 Xing, C., Liu, C., Wang, S., Chan, K.L., Gao, Y., Huang, X., Su, W., Zhang, C., Dong, Y., Fan,
886 G., and Zhang, T.: Observations of the vertical distributions of summertime atmospheric
887 pollutants and the corresponding ozone production in Shanghai, China, Atmos. Chem. Phys.,
888 17(23), **2017**.

889 Xing, J., Ding, D., Wang, S., Zhao, B., Jang, C., Wu, W., Zhang, F., Zhu, Y., and Hao, J.:
890 Quantification of the enhanced effectiveness of NO_x control from simultaneous reductions of
891 VOC and NH₃ for reducing air pollution in the Beijing–Tianjin–Hebei region, China, *Atmos.*
892 *Chem. Phys.*, 18(11):7799-814, **2018**.

893 Xu, Z., Wang, T., Xue, L.K., Louie, P.K., Luk, C.W., Gao, J., Wang, S.L., Chai, F.H., and Wang,
894 W.X.: Evaluating the uncertainties of thermal catalytic conversion in measuring atmospheric
895 nitrogen dioxide at four differently polluted sites in China, *Atmos. Environ.*, 76, 221-226, **2013**.

896 Xue, L.K., Wang, T., Gao, J., Ding, A.J., Zhou, X.H., Blake, D.R., Wang, X.F., Saunders, S.M.,
897 Fan, S.J., Zuo, H.C., Zhang, Q.Z. and Wang, W.X.: Ground-level ozone in four Chinese cities:
898 precursors, regional transport and heterogeneous processes, *Atmos. Chem. Phys.*, 14(23), 13175-
899 13188, **2014**.

900 Yang, Y., Shao, M., Wang, X., Nolscher, A.C., Kessel, S., Guenther, A., and Williams, J.:
901 Towards a quantitative understanding of total OH reactivity: A review, *Atmos. Environ.*,
902 134:147-161, **2016**.

903 Ye, L., Wang, X., Fan, S., Chen, W., Chang, M., Zhou, S., Wu, Z., and Fan, Q.: Photochemical
904 indicators of ozone sensitivity: application in the Pearl River Delta, China, *Front. Env. Sci. Eng.*
905 10(6):15, **2016**.

906 Yin, Y., Lu, H., Shan, W., and Zheng, Y.: Analysis of observed ozone episode in urban Jinan,
907 China, *Bulletin Environ. Contamination & toxico.*, 83(2), 159-163, **2009**.

908 Zhang, Q., Streets, D.G., Carmichael, G.R., He, K.B., Huo, H., Kannari, A., Klimont, Z., Park,
909 I.S., Reddy, S., Fu, J.S., Chen, D., Duan, L., Lei, Y., Wang, L.T., and Yao, Z.L.: Asian
910 emissions in 2006 for the NASA INTEX-B mission, *Atmos. Chem. Phys.*, 9(14), 5131-5153,
911 **2009**.

912 Zhang, Q., Streets, D.G., He, K., Wang, Y., Richter, A., Burrows, J.P., Uno, I., Jang, C.J., Chen,
913 D., Yao, Z., and Lei, Y.: NO_x emission trends for China, 1995-2004: The view from the ground
914 and the view from space, *J. Geophys. Res. – Atmos.*, 112(D22), **2007**.

915 Zhang, Q., Yuan, B., Shao, M., Wang, X., Lu, S., Lu, K., Wang, M., Chen, L., Chang, C.C., and
 916 Liu, S.C.: Variations of ground-level O₃ and its precursors in Beijing in summertime between
 917 2005 and 2011, *Atmos. Chem. Phys.*, 14(12), 6089-6101, **2014**.

918 Zhang, Y., Ding, A., Mao, H., Nie, W., Zhou, D., Liu, L., Huang, X., and Fu, C.: Impact of
 919 synoptic weather patterns and inter-decadal climate variability on air quality in the North China
 920 Plain during 1980-2013, *Atmos. Environ.*, 124, 119-128, **2016**.

921 Zhang, Z., Zhang, X., Gong, D., Quan, W., Zhao, X., Ma, Z., and Kim, S.J.: Evolution of surface
 922 O₃ and PM_{2.5} concentrations and their relationships with meteorological conditions over the last
 923 decade in Beijing, *Atmos. Environ.*, 108, 67-75, **2015**.

924 Zhao, C., Wang, Y., and Zeng, T.: East China plains: A “basin” of ozone pollution, *Environ. Sci.*
 925 *Technol.*, 43(6), 1911-1915, **2009**.

926 Zong, R., Yang, X., Wen, L., Xu, C., Zhu, Y., Chen, T., Yao, L., Wang, L., Zhang, J., Yang, L.,
 927 Wang, X., Shao, M., Zhu, T., Xue, L., and Wang, W.: Strong ozone production at a rural site in
 928 the North China Plain: Mixed effects of urban plumes and biogenic emissions, *J. Environ. Sci.*,
 929 doi.org/10.1016/j.jes.2018.05.003, **2018**.